

Constraints on the Velocity and Spin Dependent Exotic Interaction at the Micrometer Range

Jihua Ding,^{1,*} Jianbo Wang,^{1,*} Xue Zhou,² Yu Liu,³ Ke Sun,³ Adekunle Olusola Adeyeye,^{2,4} Huixing Fu,¹ Xiaofang Ren,¹ Sumin Li,¹ Pengshun Luo^{1,†}, Zhongwen Lan,³ Shanqing Yang,^{1,5} and Jun Luo^{1,5,‡}

¹MOE Key Laboratory of Fundamental Quantities Measurement, Hubei Key Laboratory of Gravitation and Quantum Physics, School of Physics, Huazhong University of Science and Technology, Wuhan 430074, China

²Department of Electrical and Computer Engineering, National University of Singapore,

4 Engineering Drive 3, Singapore 117583, Singapore

³School of Materials and Energy, University of Electronic Science and Technology of China, Chengdu 610054, China

⁴Department of Physics, Durham University, South Road, Durham DH1 3LE, United Kingdom

⁵TIANQIN Research Center for Gravitational Physics, School of Physics and Astronomy, Sun Yat-sen University, Zhuhai 519082, China



(Received 29 January 2020; revised manuscript received 22 March 2020; accepted 25 March 2020; published 20 April 2020)

We report on an experimental test of the velocity and spin dependent exotic interaction that can be mediated by new light bosons. The interaction is searched by measuring the force between a gold sphere and a microfabricated magnetic structure using a cantilever. The magnetic structure consists of stripes with antiparallel electron spin polarization so that the exotic interaction between the polarized electrons in the magnetic structure and the unpolarized nucleons in the gold sphere varies periodically, which helps to suppress the spurious background signals. The experiment sets the strongest laboratory constraints on the coupling constant between electrons and nucleons at the micrometer range with $f_{\perp} < 5.3 \times 10^{-8}$ at $\lambda = 5 \mu\text{m}$.

DOI: [10.1103/PhysRevLett.124.161801](https://doi.org/10.1103/PhysRevLett.124.161801)

The search for spin-dependent exotic interactions has been inspired by the physics beyond the standard model of particle physics [1–3]. One such interaction was proposed to be mediated by axions as first introduced by Moody and Wilczek [4]. The axions were initially introduced to resolve the strong CP problem [5–7] and now are considered as possible compositions of dark matter in the Universe [8–10]. Exchanging other hypothetical bosons, such as arion [11], axial photon [12], and Majoron [13], can also produce monopole-dipole or dipole-dipole interactions between fermions. Within the framework of quantum field theory, Dobrescu and Mocioiu classified the interactions by exchanging spin-0 or spin-1 bosons into 16 types [14], and 15 types of them are spin dependent. Recently, the coordinate-space nonrelativistic potentials were revisited and classified by their types of physical couplings [15].

For the spin-dependent interactions, the effect of one particle acting on another can be treated as an exotic magnetic field acting on the other particle's spin. Using the spin as a sensor, one can detect the new interactions by measuring the spin response to the exotic magnetic field, such as in experiments with magnetometers [16–20], trapped ions [21,22], nitrogen vacancy color center in diamond [23,24], and neutron or polarized ^3He atoms [25–27]. A superconducting quantum interference device was also used to probe the magnetization of paramagnetic material induced by the exotic magnetic field [28–30]. On

the other side, the spin-dependent macroscopic force or torque can be measured by using torsion balance or cantilever [31–37].

In this Letter, we report an experimental test of a spin- and velocity-dependent interaction between polarized electrons and unpolarized nucleons described by an effective potential

$$V(r) = -f_{\perp} \frac{\hbar^2}{8\pi m_e c} [\hat{\sigma} \cdot (\vec{v} \times \hat{r})] \left(\frac{1}{\lambda r} + \frac{1}{r^2} \right) e^{-r/\lambda}, \quad (1)$$

where \hbar is Planck's constant, c is the speed of light in vacuum, m_e is the mass of electron, $\hat{\sigma}$ is the spin unit vector of electron, \vec{v} is the relative velocity between the electron and nucleon, $\hat{r} = \vec{r}/r$ is a unit vector in the direction between them, and $\lambda = \hbar/m_b c$ is the interaction range with boson mass m_b . Here f_{\perp} is the dimensionless coupling constant, which could be a combination of either the scalar electron coupling (g_s^e) and the scalar nucleon coupling (g_s^N) for spin-0 exchange, or the vector electron coupling (g_v^e) and the vector nucleon coupling (g_v^N) for spin-1 exchange [14,37]. Previous experiments have been performed at the range of millimeter or above [19,25,31,32]. Constraints at the atomic scale were derived from the antiprotonic helium spectroscopy [38] and helium fine-structure spectroscopy [39] recently.

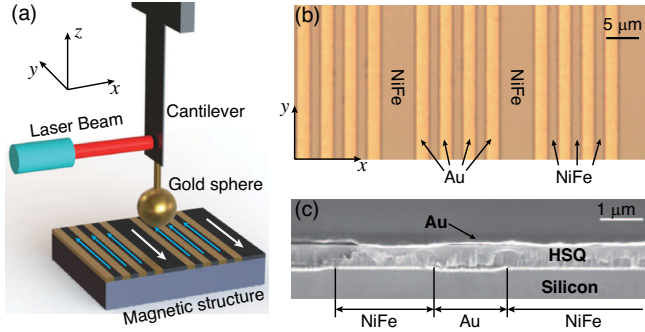


FIG. 1. (a) Schematic drawing of the experiment. Dimensions are not in scale. The arrows indicate the spin-polarization directions. The golden stripes are gold filled inside the gaps between the magnetic stripes. (b) Optical image of the structure after refilling the gaps with gold by thermal evaporation. (c) The scanning electron microscopy image of the cross section of the magnetic structure. From bottom to top, they are the silicon substrate, periodic magnetic structure, HSQ layer, and Au coating.

Here we present an experimental search at the micrometer range by measuring the lateral force between a gold sphere and a magnetic structure using a cantilever [see Fig. 1(a)]. The magnetic structure consists of periodic magnetic stripes. The magnetic stripes are magnetized in alternately antiparallel directions. The lateral force (along the x axis) is measured with the magnetic structures oscillating as $x = x_0 + A_d \cos(2\pi f_d t)$. The exotic interaction is then modulated to the high harmonics of the driving frequency f_d depending on the driving amplitude A_d . This helps to separate the spurious signals from the signal of interest in the frequency domain. Limited by the travel range of the piezo, we choose to measure the sixth harmonic component (F_{6f_d}), whose complex form is given by

$$F_{6f_d}(x_0) = -i \sum_{m=1}^{\infty} 2\pi f_d A_d \text{Im}[f(k_m) e^{ik_m x_0}] [J_5(k_m A_d) + J_7(k_m A_d)], \quad (2)$$

where $k_m = m2\pi/\Lambda$ and Λ is the magnetic structure period, $f(k_m)$ is the m th complex coefficient of the Fourier series expansion of $F(x)/v$, and $F(x)$ is the exotic force acting on the sphere as a function of x . J_5 and J_7 are the Bessel functions of order 5 and 7, respectively. It is interesting to note that the signal at $6f_d$ only has the imaginary part, as the force is proportional to the relative velocity and thus to $\sin(2\pi f_d t)$. This further helps us separate it from other forces that only contribute to the real part, such as the electrostatic, Casimir, and magnetic force. The oscillation amplitude, $A_d = 24.0 \mu\text{m}$, is chosen to maximize the signal at $6f_d$. The driving frequency of 4.3 Hz is selected to be as large as possible, but not too large to cause mechanical noise.

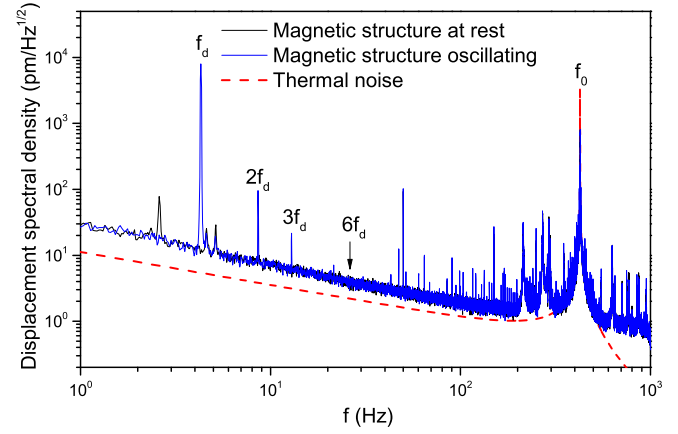


FIG. 2. Cantilever displacement spectral density measured with or without the magnetic structure oscillating. The thermal noise of the cantilever is also plotted.

The experiment was performed on a home-built scanning probe microscope as described in Ref. [40]. Data were collected using a silicon cantilever with a dimension of $430 \mu\text{m} \times 46 \mu\text{m} \times 540 \text{nm}$. A gold sphere was glued to the end of the cantilever. The gold sphere was made by melting high-purity gold wire (99.99% in purity, Goodfellow) with a diameter of $10 \mu\text{m}$. The effective spring constant of the cantilever is determined to be $3.3(3) \text{mN/m}$ using the method presented in Ref. [40]; its resonance frequency is measured to be 426Hz with a quality factor of 6134. The noise floor of the force sensor is $\sim 13 \text{fN}/\sqrt{\text{Hz}}$ at $6f_d$ as derived from the noise floor of the cantilever displacement measurement (Fig. 2). The motion of the magnetic structure does not change the noise floor of the measurement except for the peaks arising at f_d , $2f_d$, and $3f_d$.

The magnetic structures were fabricated based on $64(2)\text{-nm}$ -thick $\text{Fe}_{24}\text{Ni}_{76}$ thin films deposited on silicon substrate by magnetron sputtering. The film was protected by a $5(2)\text{-nm}$ -thick copper layer on top. Two widths of stripes were made by lithography and ion milling to achieve different coercive fields [41]. The magnetic hysteresis of the control samples with single-width stripes shows good squareness, which implies the single magnetic domain nature of the stripes. The magnetic structure consists of one wide stripe and three narrow stripes in a single period [see Figs. 1(b) and 1(c)]. This design is to balance the magnetization of alternate polarization directions, thus keeping the magnetic field in plane and close at the ends of stripes. The finite element simulations show that the magnetic force acting on the sphere by the magnetic structure is on an order of 10^{-21}N , which is negligible compared to the force sensitivity. To make the surface flat, the gaps between the stripes were first filled with gold by thermal evaporation, and then a $468(6)\text{-nm}$ -thick of hydrogen silsesquioxane (HSQ) was spin coated on the surface. The surface was further coated with a $157(7)\text{-nm}$ -thick gold to make it conductive and isoelectronic.

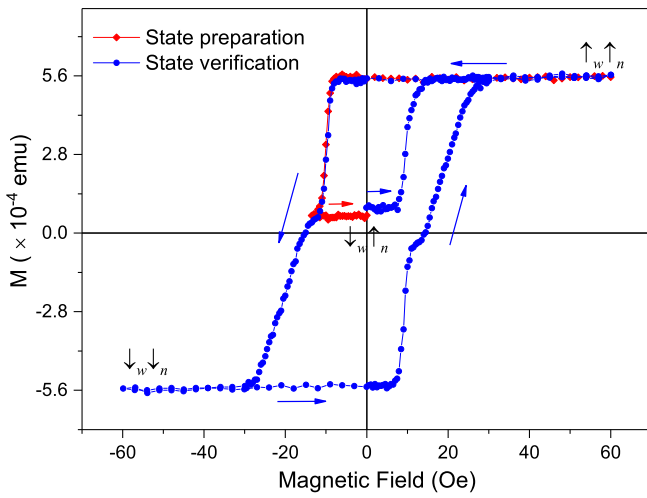


FIG. 3. Magnetic moment measurement with VSM. The arrows denote the magnetic field sweep directions. Solid diamond, state preparation prior to the experimental runs; solid circle, state verification after all the experimental runs, full magnetic hysteresis was measured afterward.

Figure 3 shows the magnetic hysteresis of the magnetic structure measured with a vibrating sample magnetometer (VSM). Because of the magnetic shape anisotropy, the wider stripe with a width of $5.92(1) \mu\text{m}$ has a smaller reverse field $H_w^c = 7 \text{ Oe}$, whereas the narrower stripe with a width of $2.02(1) \mu\text{m}$ has a larger reverse field $H_n^c = 14 \text{ Oe}$. In the full hysteresis loop, a magnetic field larger than 30 Oe can magnetize both stripes to the same direction ($\uparrow_w \uparrow_n$). The magnetization of the wide stripes starts to reverse when the field decreases to -7 Oe . The plateau around -13 Oe indicates a nearly complete

reversion of the wide stripes ($\downarrow_w \uparrow_n$), and then the narrow stripes start to reverse their magnetization when the field is below -14 Oe . A field below -30 Oe can magnetize both stripes to the reverse direction ($\downarrow_w \downarrow_n$).

Prior to the experimental runs, we prepared the magnetic structure to the antiparallel state ($\downarrow_w \uparrow_n$) by sweeping the magnetic field from 60 to -14 Oe and then to 0 Oe (solid diamonds in Fig. 3). The antiparallel state was verified by measuring the hysteresis from zero field after all experimental runs (solid circles in Fig. 3). We can see that the magnetic moment at zero field is close to the value when we prepared the state, which demonstrates that the antiparallel state has been maintained through the experiments. The magnetic moment is slightly above the initial value, due to possible relaxation of the magnetic moments around the edges and ends of the wide stripes.

Two dimensional (2D) maps of the force signal (F_{6fd}) have been measured with the gold sphere at a certain distance away from the magnetic structure. The real and imaginary components were obtained by fast Fourier transformation (FFT) of 20-s-long data recorded at every equilibrium position (x_0, y_0) when the magnetic structure was oscillating about it. Data have been taken at four areas across the surface with a lateral distance up to several hundreds of micrometers. All maps show similar characteristics as presented in Fig. 4. The maps of the real parts show some pattern whose contrast decreases with distance. The pattern is similar to what we observed in Ref. [40], which is mainly due to the patch electrostatic effect. Fortunately, for the type of the interaction we are looking for, the signal appears only in the imaginary part, according to Eq. (2). In contrast to the real parts, the maps of the imaginary parts show nearly white noise background with standard

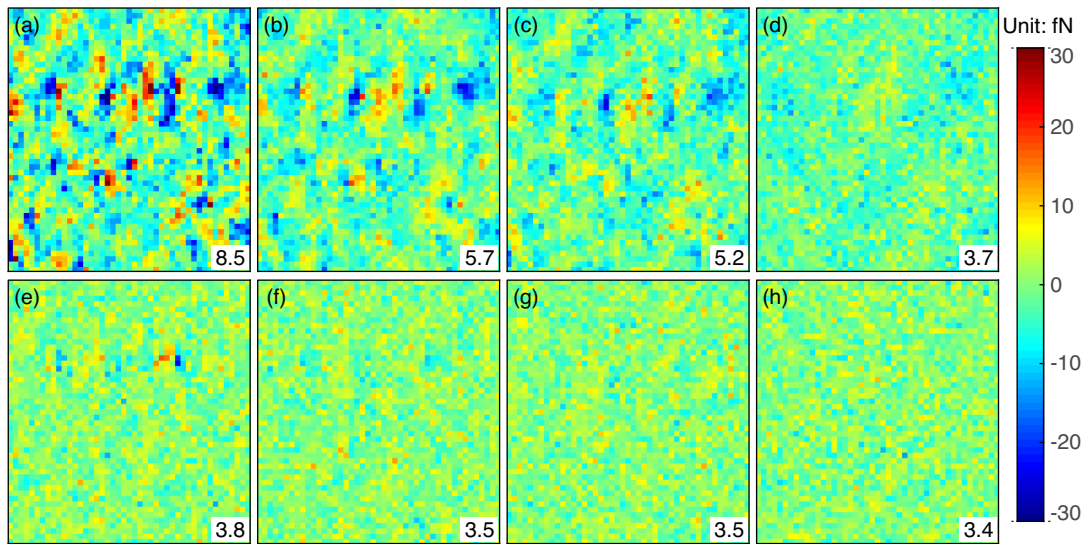


FIG. 4. 2D maps of the real part of the force signal were measured at distances of (a) 0.96 , (b) 1.17 , (c) 1.31 , and (d) $2.38 \mu\text{m}$. Their corresponding imaginary parts are presented in (e)–(h). Each pixel represents a measurement at an equilibrium position (x_0, y_0) . The standard deviation of each map is indicated in the lower right corner. The image size is $45 \times 49 \mu\text{m}$, and the horizontal direction is along the x axis.

TABLE I. Mean values and uncertainties of the main experimental parameters.

| Parameter | Value | Error | Unit |
|---|-------|-------|----------------------|
| Sphere radius | 12.26 | 0.03 | μm |
| Period of structure | 20.46 | 0.08 | μm |
| Width of the wide stripe | 5.92 | 0.01 | μm |
| Width of the narrow stripe | 2.02 | 0.01 | μm |
| Fe ₂₄ Ni ₇₆ thickness | 64 | 2 | nm |
| Spin density of the wide stripe | 6.3 | 0.7 | $10^{28}/\text{m}^3$ |
| Spin density of the narrow stripe | 8.8 | 0.3 | $10^{28}/\text{m}^3$ |
| Distance | 0.96 | 0.04 | μm |
| Drive amplitude | 24.0 | 0.2 | μm |

deviation close to the noise floor of the sensor with a 20 s integration time (~ 3 fN). The standard deviation at the distance of $0.96 \mu\text{m}$ is slightly higher than the others, probably due to a fractional contribution from the increased real components as a result of the initial phase error in FFT calculations. In general, we observe no periodic pattern as expected for an exotic interaction, and thus no such interaction should exist to the level of current experimental precision.

To set constraints on the coupling strength of the exotic interaction, we analyze the data with maximum likelihood estimation [40]. The probability density of observing the 2D map is calculated as a function of the position offset x_{00} and the coupling strength f_{\perp} for every λ according to

$$P(x_{00}, f_{\perp}, \lambda) = \frac{1}{A} \prod_{i,j} \frac{1}{\sqrt{2\pi}\sigma_{ij}} e^{-[F_{ij}^{\text{exp}} - F_{ij}^T(f_{\perp}, \lambda)]^2 / 2\sigma_{ij}^2}, \quad (3)$$

where A is the normalization coefficient, F_{ij}^{exp} , $F_{ij}^T(f_{\perp}, \lambda)$, and σ_{ij} are the measured value, theoretical value, and measurement error at pixel (i, j) , respectively. The measurement errors are mainly contributed from the noise floor of the force sensor. For every λ , the theoretical values are calculated using Eq. (2), where $F(x)/v$ are first calculated and then its Fourier coefficients $f(k_m)$ are calculated both numerically. The experimental parameters used for the calculation are listed in Table I. Conservatively, we use the 1σ bound values of the experimental parameters to obtain smaller theoretical values for certain f_{\perp} . The probability as a function of f_{\perp} is obtained by integrating out x_{00} , and then the up-bound of f_{\perp} at 95% confidential level is derived for every λ .

For simplicity, we assume that the coupling constants are identical for protons and neutrons, and the nucleon density is calculated from the density of pure gold ($19.3 \text{ g}/\text{cm}^3$). The electron spin density $\rho_{w,n}$ of the stripes are estimated from the magnetic measurements, which are given by

$$\rho_{w,n} = \frac{M_{w,n} r_{so}}{\mu_B}, \quad (4)$$

where r_{so} is the fractional ration of the spin to all magnetic moments, μ_B is the Bohr magneton, and $M_{w,n}$ is the

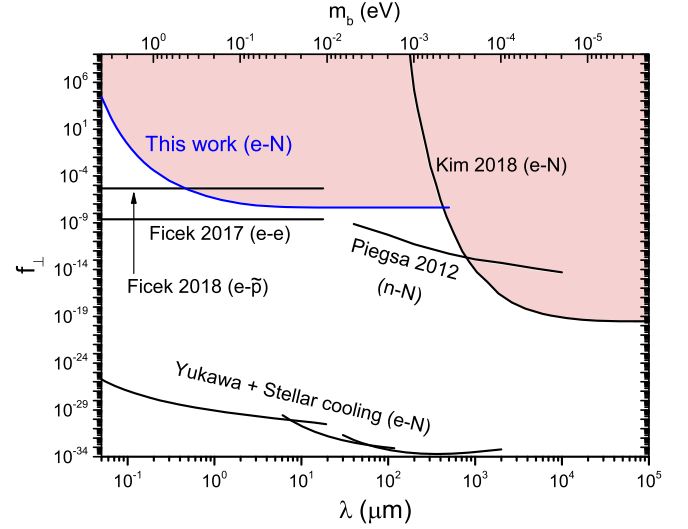


FIG. 5. Constraints on the dimensionless coupling constants f_{\perp} . Results from previous experiments are also included [19,25,38,39,43].

magnetization of the wide and narrow magnetic stripes in the antiparallel state. We use the magnetic measurement data collected after the experimental runs for the estimation and reasonably assume that the magnetization is saturated for the narrow stripes based on the measurements on the control samples of single width. On the other hand, the measured magnetization is contributed from both the spin and orbital magnetic moments of Fe and Ni atoms. The fraction of the spin moments is estimated to be 94% based on the data presented in Ref. [42].

The constraints on the coupling constants are derived from the data with a distance of $0.96 \mu\text{m}$ and are plotted in Fig. 5 in comparison with previous results. This Letter sets the strongest laboratory constraints on the interaction between electrons and nucleons at interaction range below $\sim 400 \mu\text{m}$, which corresponds to a mediated boson mass above $50 \mu\text{eV}$. Above that range, the strongest constraints are set by the experiment with a spin-exchange relaxation-free magnetometer [19]. Other experimental constraints have been obtained on the interaction between neutrons and nucleons from the neutron precession measurement [25] and on the interactions between electrons and electrons, and between electrons and antiprotons from the atomic spectroscopic measurements [38,39]. The strongest constraints are still set by a combination of g_s^e derived from the stellar cooling rate [43] and g_s^N from recent experimental tests of the hypothetical Yukawa interactions [44–46]. However, the astrophysical bounds on g_s^e may suffer from various uncertainties [47].

In conclusion, we have performed an experimental test on the spin- and velocity-dependent exotic interaction and obtained the strongest laboratory constraints on the electron-nucleon interaction below $\sim 400 \mu\text{m}$. To modulate the signal of interest and reduce the normal magnetic

force, a periodic magnetic structure with alternative spin polarizations has been used. This method would be valuable for future search for the spin-dependent interactions. The experimental sensitivity is currently limited by the noise floor of the force sensor, which is instead limited by the displacement measurement sensitivity of the interferometer. Except for the improvement of the force sensitivity, future improvements could be achieved by using larger relative velocity through improving the mechanical stability of the measurement setup.

We thank W. M. Snow, J. C. Long, H. Yan, H. B. Chan, R. W. Li, G. Klimchitskaya, and V. Mostepanenko for useful discussions. This work was supported by the National Natural Science Foundation of China under Contracts No. 11875137, No. 91736312, No. 91436212, and No. 11722542.

*These authors have contributed equally to this work.

†pluo2009@hust.edu.cn

‡junluo@mail.sysu.edu.cn

- [1] E. G. Adelberger, J. H. Gundlach, B. R. Heckel, S. Hoedl, and S. Schlamminger, *Prog. Part. Nucl. Phys.* **62**, 102 (2009).
- [2] W.-T. Ni, *Rep. Prog. Phys.* **73**, 056901 (2010).
- [3] M. S. Safronova, D. Budker, D. DeMille, D. F. J. Kimball, A. Derevianko, and C. W. Clark, *Rev. Mod. Phys.* **90**, 025008 (2018).
- [4] J. E. Moody and F. Wilczek, *Phys. Rev. D* **30**, 130 (1984).
- [5] R. D. Peccei and H. R. Quinn, *Phys. Rev. Lett.* **38**, 1440 (1977).
- [6] S. Weinberg, *Phys. Rev. Lett.* **40**, 223 (1978).
- [7] F. Wilczek, *Phys. Rev. Lett.* **40**, 279 (1978).
- [8] L. J. Rosenberg and K. A. van Bibber, *Phys. Rep.* **325**, 1 (2000).
- [9] J. E. Kim and G. Carosi, *Rev. Mod. Phys.* **82**, 557 (2010).
- [10] D. J. E. Marsh, *Phys. Rep.* **643**, 1 (2016).
- [11] A. A. Ansel'm, *JETP Lett.* **36**, 55 (1982).
- [12] P. C. Naik and T. Pradhan, *J. Phys. A* **14**, 2795 (1981).
- [13] D. Chang, R. N. Mohapatra, and S. Nussinov, *Phys. Rev. Lett.* **55**, 2835 (1985).
- [14] B. A. Dobrescu and I. Mocioiu, *J. High Energy Phys.* **11** (2006) 005.
- [15] P. Fadeev, Y. V. Stadnik, F. Ficek, M. G. Kozlov, V. V. Flambaum, and D. Budker, *Phys. Rev. A* **99**, 022113 (2019).
- [16] G. Vasilakis, J. M. Brown, T. W. Kornack, and M. V. Romalis, *Phys. Rev. Lett.* **103**, 261801 (2009).
- [17] K. Tullney, F. Allmendinger, M. Burghoff, W. Heil, S. Karpuk, W. Kilian, S. Knappe-Grüneberg, W. Müller, U. Schmidt, A. Schnabel, F. Seifert, Y. Sobolev, and L. Trahms, *Phys. Rev. Lett.* **111**, 100801 (2013).
- [18] M. Bulatowicz, R. Griffith, M. Larsen, J. Mirijanian, C. B. Fu, E. Smith, W. M. Snow, H. Yan, and T. G. Walker, *Phys. Rev. Lett.* **111**, 102001 (2013).
- [19] Y. J. Kim, P.-H. Chu, and I. Savukov, *Phys. Rev. Lett.* **121**, 091802 (2018).
- [20] W. Ji, Y. Chen, C. Fu, M. Ding, J. Fang, Z. Xiao, K. Wei, and H. Yan, *Phys. Rev. Lett.* **121**, 261803 (2018).
- [21] D. J. Wineland, J. J. Bollinger, D. J. Heinzen, W. M. Itano, and M. G. Raizen, *Phys. Rev. Lett.* **67**, 1735 (1991).
- [22] S. Kotler, R. Ozeri, and D. F. J. Kimball, *Phys. Rev. Lett.* **115**, 081801 (2015).
- [23] X. Rong, M. Wang, J. Geng, X. Qin, M. Guo, M. Jiao, Y. Xie, P. Wang, P. Huang, F. Shi, Y.-F. Cai, C. Zou, and J. Du, *Nat. Commun.* **9**, 739 (2018).
- [24] X. Rong, M. Jiao, J. Geng, B. Zhang, T. Xie, F. Shi, C.-K. Duan, Y.-F. Cai, and J. Du, *Phys. Rev. Lett.* **121**, 080402 (2018).
- [25] F. M. Piegsa and G. Pignol, *Phys. Rev. Lett.* **108**, 181801 (2012).
- [26] H. Yan and W. M. Snow, *Phys. Rev. Lett.* **110**, 082003 (2013).
- [27] H. Yan, G. A. Sun, S. M. Peng, Y. Zhang, C. Fu, H. Guo, and B. Q. Liu, *Phys. Rev. Lett.* **115**, 182001 (2015).
- [28] T. C. P. Chui and W.-T. Ni, *Phys. Rev. Lett.* **71**, 3247 (1993).
- [29] W.-T. Ni, S.-S. Pan, H.-C. Yeh, L.-S. Hou, and J. Wan, *Phys. Rev. Lett.* **82**, 2439 (1999).
- [30] N. Crescini, C. Braggio, G. Carugno, P. Falferi, A. Ortolan, and G. Ruoso, *Phys. Lett. B* **773**, 677 (2017).
- [31] B. R. Heckel, C. E. Cramer, T. S. Cook, E. G. Adelberger, S. Schlamminger, and U. Schmidt, *Phys. Rev. Lett.* **97**, 021603 (2006).
- [32] B. R. Heckel, E. G. Adelberger, C. E. Cramer, T. S. Cook, S. Schlamminger, and U. Schmidt, *Phys. Rev. D* **78**, 092006 (2008).
- [33] G. D. Hammond, C. C. Speake, C. Trenkel, and A. P. Patón, *Phys. Rev. Lett.* **98**, 081101 (2007).
- [34] S. A. Hoedl, F. Fleischer, E. G. Adelberger, and B. R. Heckel, *Phys. Rev. Lett.* **106**, 041801 (2011).
- [35] B. R. Heckel, W. A. Terrano, and E. G. Adelberger, *Phys. Rev. Lett.* **111**, 151802 (2013).
- [36] W. A. Terrano, E. G. Adelberger, J. G. Lee, and B. R. Heckel, *Phys. Rev. Lett.* **115**, 201801 (2015).
- [37] T. M. Leslie, E. Weisman, R. Khatiwada, and J. C. Long, *Phys. Rev. D* **89**, 114022 (2014).
- [38] F. Ficek, P. Fadeev, V. V. Flambaum, D. F. J. Kimball, M. G. Kozlov, Y. V. Stadnik, and D. Budker, *Phys. Rev. Lett.* **120**, 183002 (2018).
- [39] F. Ficek, D. F. J. Kimball, M. G. Kozlov, N. Lefter, S. Pustelny, and D. Budker, *Phys. Rev. A* **95**, 032505 (2017).
- [40] J. B. Wang, S. G. Guan, K. Chen, W. J. Wu, Z. Y. Tian, P. S. Luo, A. Z. Jin, S. Q. Yang, C. G. Shao, and J. Luo, *Phys. Rev. D* **94**, 122005 (2016).
- [41] S. Goolaup, A. O. Adeyeye, N. Singh, and G. Gubbiotti, *Phys. Rev. B* **75**, 144430 (2007).
- [42] B. Glaubitz, S. Buschhorn, F. Brüßing, R. Abrudan, and H. Zabel, *J. Phys. Condens. Matter* **23**, 254210 (2011).
- [43] G. Raffelt, *Phys. Rev. D* **86**, 015001 (2012).
- [44] Y.-J. Chen, W. K. Tham, D. E. Krause, D. López, E. Fischbach, and R. S. Decca, *Phys. Rev. Lett.* **116**, 221102 (2016).
- [45] W.-H. Tan, A.-B. Du, W.-C. Dong, S.-Q. Yang, C.-G. Shao, S.-G. Guan, Q.-L. Wang, B.-F. Zhan, P.-S. Luo, L.-C. Tu, and J. Luo, *Phys. Rev. Lett.* **124**, 051301 (2020).
- [46] J. G. Lee, E. G. Adelberger, T. S. Cook, S. M. Fleischer, and B. R. Heckel, *Phys. Rev. Lett.* **124**, 101101 (2020).
- [47] P. Jain and S. Mandal, *Int. J. Mod. Phys. D* **15**, 2095 (2006).